

Light Transport Acquisition via Selective Light Path Measurement

TAKAFUMI IWAGUCHI^{1,a)} TAKUYA FUNATOMI¹ HIROYUKI KUBO¹ KENICHIRO TANAKA¹
YASUHIRO MUKAIGAWA¹

Abstract: An active measurement, that senses the scene with a camera under controlled illumination, is one of the common techniques in computer vision field. Most of the conventional techniques rely on ideal light transport, or a response to the illumination of the scene. However, since an actual light transport depends on scene geometry and light behavior, undesired light transport such like inter-reflections and scattering could degrade the measurement. The goal of this thesis is to acquire desired light transport for further application such like to analyze the light behavior, to visualize the meaningful information, and to capture the appearance of objects in the real world, that are important tasks in the field of computer vision and computer graphics. To acquire the desired light transport, we focus on the light path from a light source to a sensor cell in the camera. In the conventional imaging, since the camera forms image by integrating all the light to sensor cells from various directions during exposure, the information of each path is lost. In order to acquire light transport before integration, we propose a selective path measurement. We control illumination and exposure to specify the path for the measurement. Our contribution also includes the proposal of the analysis and the application of the light transport.

1. Introduction

An active measurement, that senses the scene with a camera under controlled illumination, is one of the common techniques in computer vision field, such like the active stereo [1], [2], as in the photometric stereo [3], [4], and imaging radar [5]. The conventional active measurement techniques computes results from captured images. Light transport is a key factor of the active measurement. Illustration of light transport is shown in Fig. 1. Let us consider a case that we perform the active measurement of the scene. Multiple light sources and multiple photo-detectors (camera sensor can be regarded as an array of photo-detectors) are used for the measurement. Light evolves after it starts from a light source, interacts with the scene, and then finally is observed by photo-detectors. Light transport is a response of the scene to the incident light that describes a relationship between the incident light and the outgoing light.

The acquisition of light transport is important task in the fields of both computer vision and computer graphics for its application. The light transport itself is a great clue for understanding light behaviors such like diffuse reflections, diffuse and specular inter-reflections, and subsurface scattering in the scene. In active measurement, the result, (depth or normal) is computed from the light transport. Light transport is also applied for image-based relighting that allows us to synthesize an image of the scene relighted with the arbitrary illumination. A goal of this thesis is to

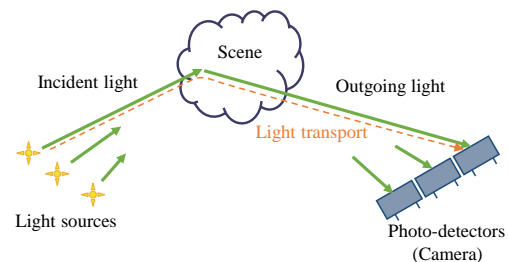


Fig. 1 Illustration of light transport. Light transport describes the relationship between incident and outgoing light.

acquire the light transport for further applications.

The light transport is complicated process relating to optical phenomenon and scene geometry. This makes its acquisition and analysis difficult. We describe this problem by taking Fig. 2 for an example. The most of the conventional techniques rely on the ideal measurement. For example, the active stereo techniques assume diffuse reflection on the surface from the direct illumination. Since inter-reflection between multiple objects (in the yellow line) is not following the assumption, it cause the wrong estimation. Also, the scattering in translucent material (in the orange line) degrades the estimation since it exhibit different response to the illumination. To deal with these problems, the patterns that is prone to inter-reflection have been proposed [6], or polarization has been utilized for descattering [7], [8], [9], however, they have disadvantages that the former only deals with long-range inter-reflection, and latter tends to be suffered from bad signal-to-noise ratio. Moreover, the desired light transport is different for its purpose. The acquisition of desired light transport is always an open problem.

¹ Nara Institute of Science and Technology, Nara, Japan

^{†1} Presently with Kyushu University

^{a)} iwaguchi@ait.kyushu-u.ac.jp

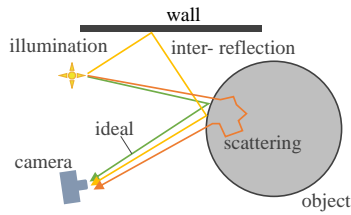


Fig. 2 Beside ideal light transport (green), there is undesired light transport caused by inter-reflections (yellow), or scattering (orange).

Another problem is how to utilize the acquired light transport for analysis and application. Since the acquired light transport and its analysis are closely related, the analysis specific to the light transport is required.

1.1 Contributions

For acquisition of the desired light transport, we focus on a light path of the light transport. Let us review Fig. 2. Light paths of the light transport are shown in green, yellow, and orange lines. While all the paths connect the illumination and the camera, they are different due to the interaction with the scene. This implies that we can acquire light transport separately if we measure the light along each path selectively.

In this thesis, we propose a **light transport acquisition by measuring light paths selectively** so that we filter desired paths from all the paths involve; we can analyze the specific behavior of the light, and take away undesired paths. The methodology of the light transport acquisition depends on the target object and the characteristic of desired paths. We specify paths by considering the geometry and the measurement setup, and selectively acquire the light transport along the path.

In order to describe our concept, we compare our method with the conventional imaging by a camera as shown in Fig. 3 (a). Since light from multiple light sources interact with the scene differently, the light travel through different paths in green, yellow, and orange, and received by the same sensor cell. In the camera, image is formed by integrating all the light to sensor cells from various directions during exposure. This means the original information of received light through each path, such as direction and change of radiation is lost. Therefore, the light transport along each path is not recovered from the images. In the presence of inter-reflection and scattering, the active measurement using conventional imaging fails. In selective path measurement, we specify each path by controlling illumination and exposure as illustrated in Fig. 3 (b). The sensor cell only receives the light from ideal path (green), the desired light transport is acquired.

We tackle two problem setting in this thesis; (1) an optical tomography of the diffuse surface object and (2) the light transport acquisition in projector-camera system.

Both types of light transport are illustrated in Fig. 4. A major difference of two types of light transport is a coordinate system that define the light transport. In (1), light transport is defined by the incident and outgoing points, which are defined on the object’s surface as shown in Fig. 4(a). This definition is appropriate for analyze the light transport in the single object, regardless of

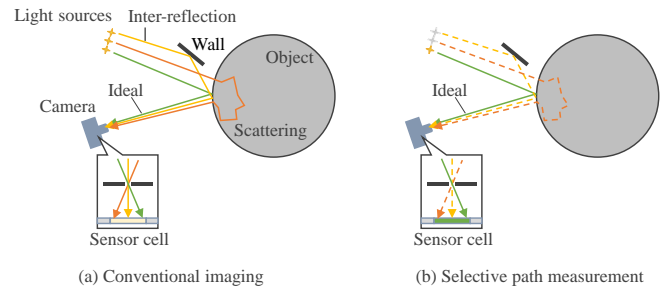


Fig. 3 Schematic illustration of selective path measurement. In conventional imaging (a), different light paths can reach a single sensor cell that output a single value. We measure a radiance of light through a specific path (b) in our framework.

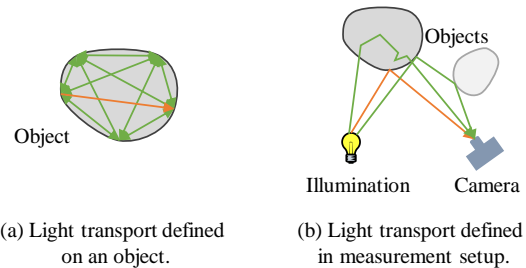


Fig. 4 Definition of our target light transport. We focus on light transport in the objects in (a) and light transport in a measurement setup in (b).

the measurement setup. Our target is called a diffuse surface object who has diffuse surface and transparent body. We propose a novel acquisition specialized for the diffuse surface object. In (2), the light transport is defined in a measurement setup as shown in Fig. 4(b). This definition is appropriate for analyze the light transport in the scene with multiple objects. It is still usable to analyze the light transport in the object, however, the geometric relationship must be considered. We acquire two different types of the light transport, called plane-to-ray light transport and full light transport, respectively. The acquisitions is made according to the light transport distance by utilizing a novel synchronized projector camera system.

Another contribution of this thesis is **the proposal of the analysis and the application of the light transport**. In (1), the interior of the object is reconstructed from the light transport. To reconstruct the interior, we propose a light path model inside the object and the reconstruction algorithm. In (2), we show various application of plane-to-ray and full light transport. We show the light transport allows us to visualize and to analyze in efficient way.

2. Light transport acquisition of diffuse surface object [10], [11]

2.1 Introduction

The measurement of an object’s interior is important in various applications, such as the detection of foreign objects in food and the inspection of the human body in a medical examination. An optical measurement is a safe inspection technology that does not use X-rays and has no risk posed by a radiation dose. Furthermore, optical measurement provides functional information on optical properties; e.g., blood flow is estimated from spectral ab-

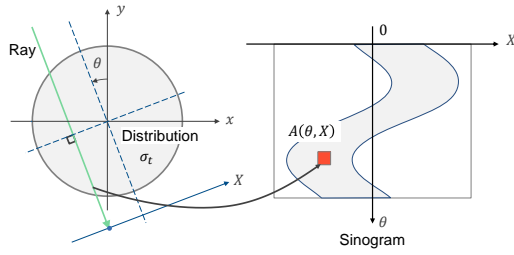


Fig. 5 Relation between the path and sinogram coordinates. Total attenuation along a ray is stored in a specific coordinate in sinogram.

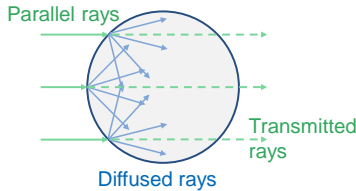


Fig. 6 When parallel rays are cast, they spread at the incident points on the surface.

sorption. One of the challenging problem of optical measurement is optical tomography. Like X-ray Computed Tomography (CT), optical tomography measures an 3-dimensional internal structure or interior of objects using optics.

In the tomography, the interior is estimated from the transport measured by sensors surrounding the object, rather than is measured directly. There are two requirements to reconstruct the distribution from the transport. First, the path model of the transport is required to transform the measured transport into the distribution. Second, a measurement technique is required so that the transport along the specific path considered in the model is measured.

We aim to acquire light transport according to a path model so that the interior is reconstructed from the acquired light transport. We target objects that has a diffuse surface and an interior that is assumed transparent, where light is absorbed but not scattered. Fruits like grapes, light bulbs with white glass, and hollow plastic bottles are examples of such objects.

In this section, we propose a *shortest path model* that assume the light travels shortest distance in the diffuse surface object as a light path model in the diffuse surface object. We propose selective path measurement for light transport acquisition according to the model. We also propose a reconstruction method of interior from acquired light transport. Our contribution also includes coverage analysis of measurement and a design of measurement setup.

2.2 Acquisition of light transport inside diffuse surface object

2.2.1 Radon transform

We reconstruct a distribution of the absorption coefficient σ of the target's interior. The absorption coefficient represents how much light is absorbed as light travels a unit distance. We now define the total absorption A by following Lambert-Beer law, as the logarithm of I_o (the intensity of light after light travels through the target) divided by I_i (the intensity of light before entering the

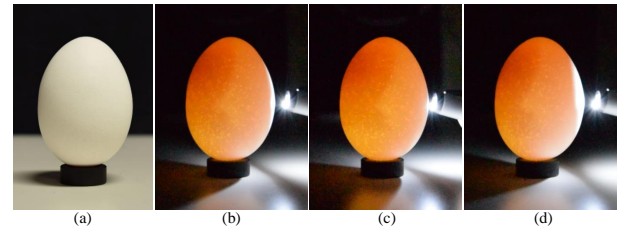


Fig. 7 Observation of an egg using LED pointer. The silhouette of yolk appears on the opposite side of illuminated point.

target):

$$A = \log I_o - \log I_i. \quad (1)$$

The relationship between the total absorption and absorption coefficient is described by the *Radon transform*. For a simplicity, we consider the problem in two dimensions. When a ray propagates through an area Ω , the total absorption is an integral of the absorption coefficient along the path:

$$A_\Omega = \iint_{x,y \in \Omega} \sigma(x,y) dx dy. \quad (2)$$

The path of a ray is generally assumed straight in the Radon transform. Let us describe a straight ray in polar coordinates fixed on the object as illustrated in Fig. 5. A radon transform about a ray (X, θ) is written as

$$A(\theta, X) = \int_{-\infty}^{\infty} \sigma(z \sin \theta + X \cos \theta, -z \cos \theta + X \sin \theta) dz. \quad (3)$$

We reconstruct a distribution of the absorption coefficient using the inverse Radon transform that is derived from Eq. (3). The reconstruction of the interior requires the total absorption of rays passing through the interior (i.e., $A(\theta, X)$) for all possible θ and X . Ideally, these rays are acquired by measuring the transmitted rays when parallel rays are cast toward the target from various angles. This method works well when the paths of rays are not disturbed by the target as in the case of X-rays. However, as illustrated in Fig. 6, each ray entering the object spreads when the target has a diffuse surface. The transmitted rays are no longer parallel and it is difficult to determine paths of the measured rays.

2.2.2 Shortest path model

We model light paths in a diffuse surface object as a first step to determining the paths of rays. We discuss about the light path model by taking an egg in Fig. 7 as an example. An egg consists of a shell, white and yolk. In order to inspect the egg, we illuminate the shell with a LED pointer. When the shell is illuminated from a right side, a silhouette of yolk appears on a left side as shown in Fig. 7(b). And the silhouette moves corresponding to the moving illumination as shown in Fig. 7(b), (c) and (d). We consider how the silhouette appears by using an illustration of this observation (Fig. 8). When light ray from the pointer hit surface of the shell, it should diffuse and should form spreading paths from the incident point. These paths are mostly straight, since the white should be weak scattering media. Then rays travel through yolk should be attenuated and the others should not, as a result they make such a silhouette.

We generalize this observation as a model. In this model,

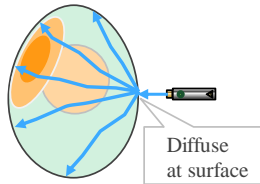


Fig. 8 Illustration of an egg observation. Spread rays at surface make the silhouette.

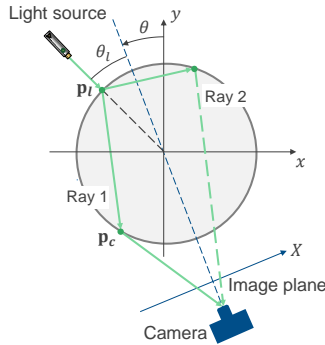


Fig. 9 Setup of the measurement. Light source and camera are pointing to the center of rotation.

we assume light diffuse at the incident point and travel straight through medium. Therefore, paths in the object are regarded as a set of straight rays spreading from the incident point as illustrated in Fig. 10. Since the straight path inside the object travels shortest distance in the object, the model is called *shortest path model*.

2.2.3 Setup of the measurement

Because the light path is modeled as a straight line, a path in the object is uniquely determined if both ends of the path are specified. If there is light in a large area, which means many rays are cast as illustrated in Fig. 6, the exact point that a ray enters is difficult to determine. Incident light should fall in a small area to avoid this problem. Meanwhile, rays exiting the object are measured by shooting the surface of the target. The shooting is repeated while the object is rotated to collect rays entering at and exiting from various points. Accordingly, a setup will consist of a narrow light source, camera, and rotary stage on which the target is placed, as shown in Fig. 9.

We assume the orthogonal projection or perspective projection as the projection model of the camera. In the case of orthogonal projection, point of incident and outgoing ray are determined with regardless to the placement of the object and camera. Meanwhile, it requires a special optics like telecentric lens, moreover, it cannot handle with the objects bigger than the size of the lens. In the case of the perspective projection, while the placement of the object and camera must be taken into account, lens is off-the-shelf and it is easier to measure big object thanks to the wide Field of View (FOV).

2.2.4 Light path alignment

A raw measurement must be converted into light transport to reconstruct interior. We call this conversion *light path alignment*. Geometry of light path and change of intensity are considered in light path alignment.

First, we discuss about the geometry of light path. Paths of a ray in a three-dimensional scene should be computed because

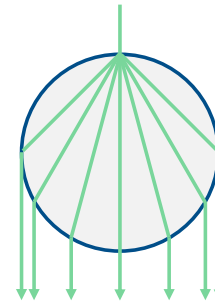


Fig. 10 In shortest-path model, the rays are modelled as straight in the body after diffusion on the incident point.

they are required for the reconstruction. The three-dimensional coordinates of the points at which a ray enters and exits are determined as follows. The point at which a ray enters is determined by calculating the intersection of the ray from the light source and a contour of the target. Similarly, the point at which a ray exits is determined by calculating the intersection of the ray from the camera and a contour of the target. To uniquely determine these intersections of the ray and the contour of the target, all the contours of the target must not be occluded from the light source or the camera. Therefore, the shape of the object need to be convex in our measurement. To obtain a target contour, we compute a visual hull [12] as the shape of the target in the following steps. In order to capture the silhouette of the target, we place the diffuse plane behind the target from the camera view and illuminate the plane so that it looks evenly illuminated. A silhouette is then extracted by binarization after subtracting the background from the captured image. A visual hull is finally computed by taking an intersection of the perspective projection of the silhouette on the object space. Since our measurement needs the shape of the target to be convex, it is reasonable to utilize a visual hull that is only applicable for convex shapes.

The geometry of light paths also affects the intensity of rays. A intensity distribution through the surface is described by the bidirectional transmission distribution function (BTDF) $f_T(\omega_i, \omega_o)$, where ω_i is the incidence angle and ω_o is the outgoing angle of the light. For accurate reconstruction, the effect at the surface must be compensated. To compensate this effect, $f_T(\omega_i, \omega_o)$ within sampling range must be measured additionally. A intensity of light transport inside the object is computed by cancelling BTDF. Also, refraction at the surface also affects the intensity where the effect is governed by Fresnel equation. We assume this effect is included in BTDF.

After light path alignment, we can employ a sinogram for the representation of acquired rays. We consider polar coordinates (X, θ) fixed on the target. The origin is at the center of rotation in the measurement setup. In a 2D representation of sinogram, horizontal and vertical axes respectively correspond to (X, θ) , and an attenuation of the ray is stored.

For each ray, we define an intersection of the ray and a contour of the object in Cartesian coordinates (x, y) that share the same origin as the polar coordinates (X, θ) . By denoting the intersection of a ray from the camera and a target by p_i and the intersection of a ray from the camera and a contour by p_c , the angle of a path θ is calculated as

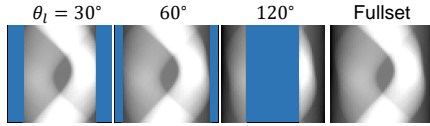


Fig. 11 Missing area of sinogram according to θ_l . While sides of sinogram are missing at $\theta_l = 30^\circ, 60^\circ$, central part is missing at 120° .

$$\theta = \arg(\mathbf{p}_l - \mathbf{p}_c), \quad (4)$$

where $\arg(\cdot)$ denotes the angle between a vector and the x -axis. A displacement of path X is calculated according to

$$X = \mathbf{p}_l^\top \cdot \begin{bmatrix} \sin \theta \\ \cos \theta \end{bmatrix}. \quad (5)$$

2.2.5 Observation rate of the light path

When the surface of the object is measured using a single camera, not all rays in the object are measured depending on the object's shape and the optical setup. We now look at Fig. 9 to understand the unobserved rays. Rays 1 and 2 cast from the light source enter the object at the same point but exit from different points, before being measured by the camera on the opposite side of the object. While ray 1 is observable because it reaches the surface visible from the camera, ray 2 is unobservable because it reaches the surface unobservable from the camera.

Let us assess the effect of unobserved rays. We simulate the measurement for the case where the camera model is perspective and the target is a cylinder and generate sinograms for different θ_l in Fig. 9. Figure 11 shows generated sinograms and the "fullset" sinogram that contains sufficient rays with which to reconstruct the full interior. There are missing areas in the sinograms owing to the unobserved rays. In the case of $\theta_l = 30^\circ$, there are missing areas on both the sides of the sinogram. Likewise, in the case of $\theta_l = 60^\circ$, there are missing areas on the sides but the areas are smaller. In contrast, a missing area appears at the center in the case of $\theta_l = 120^\circ$.

2.3 Reconstruction

When there are insufficient observations, a possible solution is to modify the setup by adding another light source or camera to complete the observation. When it is possible to observe all the paths, the interior should be reconstructed most accurately. One of the difficulties of this approach is that an additional light source or camera must be precisely aligned because the reconstruction is sensitive to misalignment. Another difficulty is that the number and the placement of the light source and the camera depend on the shape of the object. Although the optimal configuration is difficult to find, it is not usable for other objects. Moreover, there is no guarantee of the existence of the configuration that makes the observation complete.

In this paper, we employ numerical optimization to deal with the problem of incomplete observations. The numerical optimization can be used with the multiple light sources and camera.

A reconstruction from insufficient observation have been actively studied for decades in field of medical imaging, since X-ray dose can be reduced by reducing radiation, however, it sometimes causes insufficient measurement. One of the problem is

called short-scan. To reconstruct exact interior, the observation requires a scan over certain angle, however, in short-scan problem, a scan angle is not sufficient. For this problem, reconstruction using back projection with a special filter has been proposed [13], however, it is known that the reconstructed interior is not exact [14]. A approach to such problem is iterative reconstruction that iteratively update the interior to minimize re-projection error. Algebraic Reconstruction Technique [15] and Simultaneous Algebraic Reconstruction Technique [16] has been used for improving reconstruction quality. To deal with missing angles, iterative methods based on filtered backprojection have been proposed [17], [18]. Our problem is different from short-scan problem, since the scan angle is sufficient.

Our problem is more similar to so called Region of Interest (ROI) reconstruction. In this problem, X-ray radiates only to a target region inside the body. As an analytical approach, methods based on Hilbert transform reconstruct an exact interior from the truncated projection data [19], [20]. However, they requires a measurement to include a specific boundary of the target, therefore, they cannot be applied in a straightforward way for our case. Moreover, our problem setting is different since we are trying to reconstruct whole region of the target.

In our problem, the exact reconstruction should not be possible since the observation is insufficient as we discuss in a next section. In recent years, numerical optimization has been studied to estimated a realistic interior with prior knowledge. They formulate optimization problem where prior is included as regularization term or constraint. Especially, convex optimization have been studied actively since regularization or constraints on the solution can be imposed in straightforward way. Some works took this advantage to reconstruct from small number of measurement by minimizing total variation [21], and compressive sensing [22]. We follow these approach to impose constraints that are designed for our problem.

2.3.1 Formulation as an optimization problem

In the case that the observations are insufficient, the correct reconstruction is difficult because there are multiple solutions that agree with the observation mathematically. We introduce two constraints to eliminate solutions that are not physically correct and to achieve convergence to a more realistic distribution. The first constraint is the physical constraint (PC) on the range of the distribution of the absorption coefficient that is derived from the existing observations. This constraint rejects solutions that are physically wrong; however, there are still many possible distributions. The second constraint is regularization based on the total variation (TV) semi-norm that imposes smoothness on the distribution. This constraint allows convergence to a realistic solution by reducing the effect of noise of the observation.

We formulate the reconstruction as an optimization problem:

$$\arg \min_{\sigma} E(\sigma) + \iota_C(\sigma) + \lambda|\sigma|_{TV}. \quad (6)$$

The first term is a data-fidelity term that implies that a re-projection of an estimated distribution by the Radon transform should be close to a sinogram $\mathbf{A}_{observed}$. The second term is the PC on the distribution and the third term represents TV semi-norm regularization. Because the objective function of Eq. (6) is convex, we

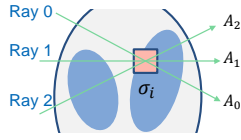


Fig. 12 Rays passing through a cell of the distribution. Absorption of the cell must be smaller than the total absorption of all the rays.

employ the alternating direction method of multipliers to solve the problem.

Reprojection error of the Radon transform To derive the reprojection error, we rewrite the Radon transform (Eq. (3)) in matrix form. Let i denote an index of a cell of a discrete distribution after serialization. A Radon transform of a ray having index j is written as

$$A_j = \sum_i r_{ij} \sigma_i, \quad (7)$$

where

$$r_{ij} = \begin{cases} 1 & (\text{if ray } j \text{ hits } \sigma_i) \\ 0 & (\text{otherwise}). \end{cases} \quad (8)$$

By combining Eq. (7) for all rays as a linear system,

$$\mathbf{A} = \mathbf{R}\boldsymbol{\sigma} \quad (9)$$

is derived. In the optimization problem, reprojection error is computed by taking the difference between \mathbf{A} and the projection of estimated $\boldsymbol{\sigma}$ obtained using matrix \mathbf{R} . We consider reprojection error only for available observations and measure it using the $L-2$ norm. Let $\mathbf{R}_{\text{observed}}$ denote the Radon transform for available observations and $\mathbf{A}_{\text{observed}}$ denote a sinogram of available observations. Finally, the data fidelity term is derived as

$$E(\boldsymbol{\sigma}) = \|\mathbf{A}_{\text{observed}} - \mathbf{R}_{\text{observed}}\boldsymbol{\sigma}\|_2^2. \quad (10)$$

Physical conditions of light absorption

The constraint is determined by the existing observations considering a physical condition of the coefficient of light absorbance. Because light does not increase in intensity as it travels through an object, the absorbance coefficient cannot be less than zero. The lower bound of the absorption coefficient σ_i is written as

$$\sigma_i \geq 0. \quad (11)$$

The upper bound of the absorbance coefficient can be determined by considering the relationship between the total absorption and the distribution of the absorbance coefficient. As Eq. (7) implies, the total absorption of a ray is the integral of the absorbance coefficient along the path. In the example presented in Fig. 12, only three light paths pass through σ_j . Therefore, σ_j must not exceed the total absorptions of the three light paths, and σ_j is thus constrained as $\sigma_j \leq \min(A_0, A_1, A_2)$. The absorption at a certain pixel must therefore not be higher than the minimum of all the projections that travel through the pixel. In the general case, the upper bound is written as

$$\sigma_j \leq \min_{i \in \chi_j} (A_i), \quad (12)$$

where χ_i is a set of rays that hit σ_j .

The lower and upper bounds form the box constraint of the

solution. Let a set C denote the range of absorption:

$$C = [\mathbf{0}, \sigma_{\max}], \quad (13)$$

where

$$\sigma_{\max} = \left(\min_{i \in \chi_1} (A_i), \min_{i \in \chi_2} (A_i), \dots, \min_{i \in \chi_N} (A_i) \right)^T. \quad (14)$$

The constraint is then represented by the indicator function $\iota_C(\boldsymbol{\sigma})$:

$$\iota_C(\boldsymbol{\sigma}) = \begin{cases} 0 & (\text{if } \boldsymbol{\sigma} \in C) \\ \infty & (\text{otherwise}). \end{cases} \quad (15)$$

Constraint about the spatial smoothness of the interior We define the TV norm $\|\cdot\|_{TV}$ as

$$\|\boldsymbol{\sigma}\|_{TV} := \sum_{i,j} \sqrt{|\nabla_1 \boldsymbol{\sigma}|^2 + |\nabla_2 \boldsymbol{\sigma}|^2}, \quad (16)$$

where ∇_1, ∇_2 are the discrete horizontal and vertical differential operators. The minimization of the norm forces the distribution to vary gradually while preserving the edges. This is preferable in most cases, and we can adjust the effect of the term by choosing a small λ whenever it is not suitable.

2.4 Experiment

2.4.1 Appropriate setup of the measurement

We determine the appropriate setup before performing an experiment in a real environment. We first investigate the characteristics of our reconstruction method based on the optimization by comparing with the conventional filtered back projection (FBP). Moreover, we compare the reconstructed interiors obtained under different setups of the measurement to evaluate the effect of the setup on the accuracy of the reconstruction. Synthetic sinograms are generated by solving the forward Radon transformation (Eq. (9)) for different θ_l . We also evaluate the interiors reconstructed by the FBP and our reconstruction method.

Fig. 13 shows the reconstructed interiors for $\theta_l = 0^\circ, 30^\circ, 60^\circ, 90^\circ,$ and 120° . In the cases of $\theta_l = 0^\circ, 30^\circ,$ and 60° , there are missing areas on both sides of the sinogram. The outer parts are not correctly estimated owing to the large missing areas at $\theta_l = 0^\circ$, but the central part is estimated correctly. There are similar tendencies in the results for $\theta_l = 30^\circ$ and 60° , but the errors are smaller because of the better observation.

It is found that our reconstruction method failed to reconstruct the center of the interior as for reconstruction by the FBP. This is because of the absence of observations of the center; no rays passing through the central area are observed, whereas more than one ray is observed in the previous cases. The whole interior needs to be reconstructed such that the center of the sinogram is not missing. In terms of quality, our method provides a better reconstruction than the FBP. Whereas the result of the FBP has line artifacts and blurring, a clear shape is reconstructed without artifacts using our method.

We now look for an appropriate setup such that the coverage of the observation is high, while the center of the sinogram remains filled. From the discussion in Sec. 2.2.5, the coverage takes its maximum at $\theta_l = \frac{\pi - \theta_{FOV}}{2}$ in the case of perspective projection,

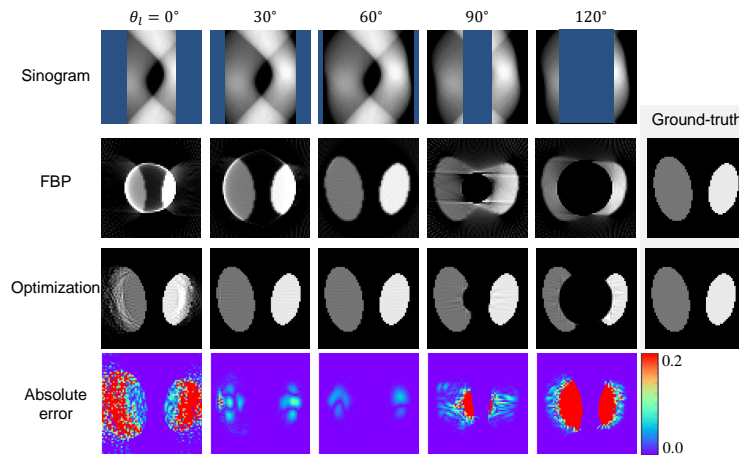


Fig. 13 Sinogram and reconstructed interior by FBP and proposed method according to setup. When sides of sinogram are missing, optimization method reconstructs all the interior which FBP fails.

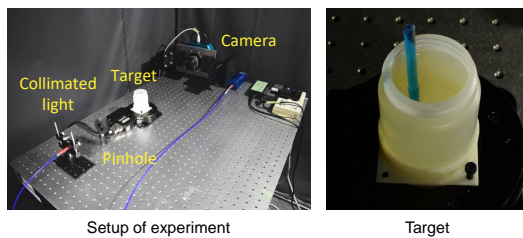


Fig. 14 Optical setup for the real world experiment. Collimated light is cast through pinhole on target on rotary stage. Camera captures images from opposite side. Our target is a plastic bin filled with gelatin. A blue plastic is stuck.

however, in the case of $\theta_l > \frac{\pi - \theta_{FOV}}{2}$, the center of the sinogram is missing. For these reasons, the appropriate setup is $\theta_l = \frac{\pi - \theta_{FOV}}{2}$; however, care needs to be taken that θ_l does not exceed the angle.

2.4.2 Experiment on a real object

In this section, we perform an experiment in a real environment to confirm the validity of the shortest-path measurement by comparing the result with a measurement made under a parallel lighting setting.

The setup is shown in Fig. 14 for the shortest-path measurement; the target on the rotary stage is illuminated by the light source and captured by the camera from various angles. The target of the experiment is a bin filled with gelatin and blue transparent plastic struck at some distance from the center of the bin. The light is collimated with a lens and is narrowed by an aperture. θ_l is fixed to 45° . We chose the angle such that the center of the sinogram is filled while the observed intensity is high enough for a quick measurement.

To calculate the total absorption, a reference object without a plastic stick is measured in addition to the target; the total absorption is then calculated by Eq. (1). Note that this calculation also cancels out the angular nonuniformity of diffusion, or BTDF of the surface. Because s_i and s_r have ω_i and ω_o in common, the bidirectional transmission distribution function f_T of the surface of the target is cancelled out.

The next step is alignment of the light path. After a contour of the target is estimated considering the visual hull of silhouettes from various views, the light path is aligned with the contour es-

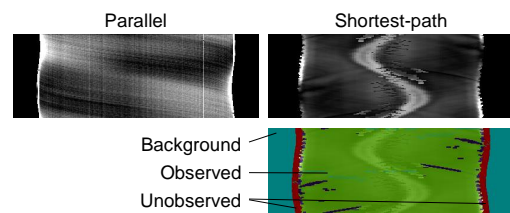


Fig. 15 Acquired sinogram under parallel lighting and proposed measurement. We clearly see the trajectory of the plastic stuck in shortest-path measurement, which is hardly seen in parallel lighting.

timated and a sinogram is generated. The interior is reconstructed from the sinogram.

For the comparison, we measure the same target under a parallel light setting. The same setup is used except that a parallel light source is cast directly and θ_l is set to 0° . The sinogram is generated directly from captured images under the assumption that rays travel straight in the target and measured transmitted rays remain parallel to each other.

Figure 15 shows sinograms of the parallel light setting and the shortest-path measurement. We cannot see an effect of plastic in the sinogram of the parallel light setting. This is because the parallel rays once diffuse at the surface when entering the target and light paths are mixed. Therefore, rays passing through the plastic are no longer distinguished. In contrast, we see a clear trajectory through the plastic in the sinogram of the shortest-path measurement. There is also blurring along the trajectory and non-zero values outside the trajectory. This should be a result of corruption of the path due to scattering in the media and reflection and refraction at the plastic's surface. We can also see small missing areas on both sides in the sinogram owing to the limitation of the measurement.

The result of reconstruction is shown in Fig. 16. From the top view of the target, the distribution of the absorption is expected as shown at top right. The red and blue lines in the figure respectively indicate the contour and the boundary between observed and unobserved areas of the sinogram.

We now look at the reconstruction of the parallel light setting that is reconstructed by the FBP. The distribution is almost uniform and we can hardly tell the area of the plastic stick. For

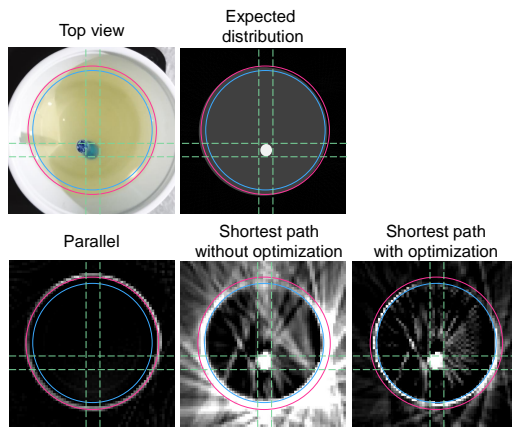


Fig. 16 Expected distribution and reconstructed interior. While the interior is not reconstructed by measurement under parallel lighting, it is reconstructed with many artifacts by proposed measurement and reconstruction method without optimization. Reconstruction method with optimization successfully reduce artifacts significantly.

the shortest-path measurement, we show two results of reconstruction obtained without optimization (i.e., the FBP) and with our optimization method. In contrast to the case for the parallel light setting, the proposed method successfully reconstructs the area of plastic stick regardless of the reconstruction method. This suggests that our path model approximates the actual paths well therefore the paths are converted to parallel by the alignment process. This confirms the validity of our assumption on light paths. There are blurry artifacts outside the plastic area that should be associated with the corrupted paths described above.

We now compare the results of the reconstruction methods. In the result of the FBP, the distribution outside the blue circle is not reconstructed and it corresponds to the missing area in the sinogram. In contrast, our optimization method is able to reconstruct the distribution where there are insufficient observations. It is confirmed that our method has an advantage over the FBP method.

3. Light transport acquisition of projector camera system [23], [24]

3.1 Introduction

In this chapter, we acquire the light transport in the projector-camera system. The projector camera system is one of the common system for the active measurement in the computer vision, used for tasks such as 3D triangulation, super-resolution, and projection-mapping.

Light transport in projector camera system is received light of camera pixels when each projector pixel is turned on. Since today’s projector and camera have high resolution, the number of sampling is enormous.

3.1.1 Distance of light transport

The light transport is characterized by the transport distance or the distance the light travels in the scene as illustrated in Fig. 17. Direct transport, that is shown in red line, is the transport of the light that bounce only once in the surface of the object as with diffuse reflections. In short range transport, that are shown in orange lines, the light that travels short distance as a result of subsurface scattering or diffuse inter-reflections. The light that travels long

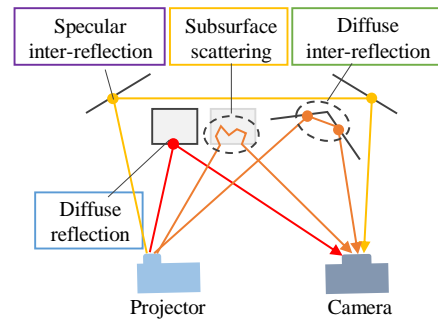


Fig. 17 The light transport is characterized by the transport distance. The transport distance depends on optical behaviours, such like diffuse reflections, diffuse inter-reflections, subsurface scattering, and specular inter-reflections.

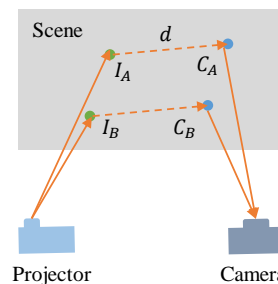


Fig. 18 Corresponding illumination for the same transport distance at different points. To acquire the light transport of the same distance at two different points, two measurements are required.

distance as with specular inter-reflections is considered as long range transport, that is shown in yellow line in the figure.

In this chapter, we aim to acquire the light transport according to its distance to analyze the light behavior in the scene. While the transport distance is meaningful information, it is difficult to acquire the light transport of the specific distance efficiently under spatially varying illumination. Let us explain this problem using Fig. 18. For the point C_A in the scene, the illumination I_A corresponds to the specific transport distance d . And for the different point C_B , the illumination I_B corresponds to the same distance. Therefore, two measurements are required to acquire the transport of the same distance for two points.

Reddy et al.[25] show the light transport can be decomposed into direct, near-range, and far-range transport (which corresponds to direct, short, and long transport respectively in our notation) components. They decompose the light transport into three components by high- and low- frequency patterns, however, their method does not acquire the light transport of the specific distance.

3.1.2 Light transport in projector camera system

In projector camera system shown in Fig. 19, light cast from the projector interacts with the scene, then received by the camera sensor. Projector send a ray to a specific pixel which is expressed as (u, v) in a projector plane and camera receive a ray through a specific pixel which is expressed as (s, t) in a sensor plane. Therefore, the light transport between projector and camera is fully expressed by 4D function $T_{full}(u, v, s, t)$.

In this chapter, the light transport distance is defined in a camera plane where 3D scene is projected. Therefore, short light

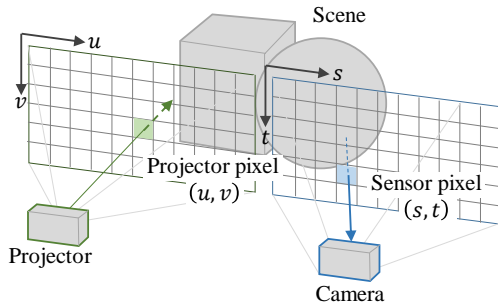


Fig. 19 Full light Transport between projector and camera is described in 4D function.

transport in our measurement does not always mean short distance in 3D coordinate. For instance, pixels which are located in close distance could point to far 3D locations at different depths. Note that short distance is 3D coordinates always satisfies short distance in our measurement unless Cartesian distance is used.

3.1.3 Our contribution

In this chapter, we propose the efficient acquisition that the light transport of the specific distance is acquired for all the sensor pixels by small number of measurements. Such acquisition is made by utilizing using *synchronized projector camera system* without any computation. We propose new imaging technique which exploits the light transport between the illumination plane and camera pixels, called *plane-to-ray* light transport. Then, we extend it to acquisition of full light transport.

3.2 Acquisition of plane-to-ray light transport

3.2.1 Epipolar geometry and light transport

We utilize the setup of synchronized projector camera system [26], that consists of a raster-scan projector and a rolling-shutter camera. The projector illuminates the scene with a plane that is swept vertically. The camera synchronizes its rolling shutter to a fixed row-offset from the illumination plane. Each camera row exposes as projector row advances, so that a single image is formed.

The Projector and camera are rectified so that their rows are aligned on the same epipolar plane. In [26], the direct and indirect transport is acquired using this alignment. Since direct light, that bounce only once in the scene, must travel through the same epipolar plane, it can only travel from projector row i to camera row i . In contrast, indirect light, that multiple times, can travel from projector row i to any camera row j except i .

This alignment also allows us to acquire the light goes through the epipolar plane which contains the projector row v and that returns through the another epipolar plane contains the camera row s . We propose a new light transport, called *plane-to-ray light transport*, characterized by the relative row offset between projector row v and camera row s .

We illustrate plane-to-ray light transport in Fig. 20. Plane-to-ray light transport is transport between the projector row v and a sensor pixel (s, t) in camera row t , that is expressed as 3D function $T_{PTR}(v, s, t)$. The row offset between projector row v and camera row s is controlled by the *synchronization delay*, the timing difference between the synchronized projector scanning and camera rolling shutter. In addition, the *exposure* of the camera row deter-

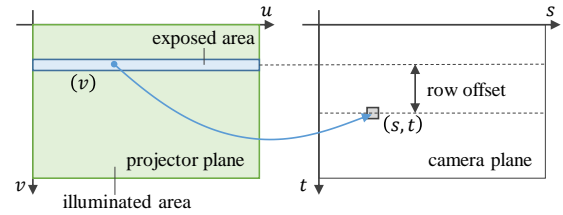


Fig. 20 We define plane-to-ray Light Transport as transport between an illuminated row and a camera pixel.

mines the width of illuminated area.

3.2.2 Efficiency of light transport acquisition for limited range

The light transport can expressed as a light transport matrix whose row corresponds to the sensor index and column corresponds to the illumination index. We discuss about the efficiency for limited range transport, by taking an example of short-range light transport.

First, we explain the order of the acquisition using a sub-matrix of the light transport matrix. In Fig. 21, we visualize the sub-matrix of the light transport matrix, where each column of the matrix is the projector row and each row is the sensor row. The diagonal elements are the direct component where the light from a row of the projector reaches the same row of the sensor. The adjacent elements in the row direction are the short-range transport.

Now, we assume the scene have the direct and short range transport that is expressed as Fig. 21(a). To explain the effectiveness of the measurement, fist, let us consider about how the transport is acquired by pixel-to-pixel measurement. In pixel-to-pixel measurement, a pixel of the projector is turned on, and all the sensor pixel is exposed with global-shutter. Each acquisition fills a column of the matrix (Fig. 21(b)). Therefore, it requires all the rows to be acquired to obtain the direct and the short-range transport. In contrast, our method acquires an oblique elements in each capture (Fig. 21(c)). It requires only few captures to acquire the direct and the short-range transport.

There is a trade-off between the range of transport captured at once and the number of captures. In short, both methods require the same number of captures to acquire all the element of the matrix. Our method is beneficial when the range of the transport is limited as for short-range transport.

Short-range transport is also assumed in [27]. They parallelized the acquisition by subdividing the projector pixels into blocks to make sure a sensor pixel is affected by only one illumination block. In our method, there is always only one illuminated row, thus no need to subdivide the projector rows.

3.3 Acquisition of full light transport

We extend acquisition of plane-to-ray light transport to the acquisition of the full light transport. In the acquisition of plane-to-ray light transport, a white pattern is projected to illuminate all the pixels in the projector row. To acquire the light transport from a pixel from the projector instead of a projector row, we project a vertical line instead of the white pattern as shown in Fig. 22. Since a pixel is only illuminated during exposing a camera row

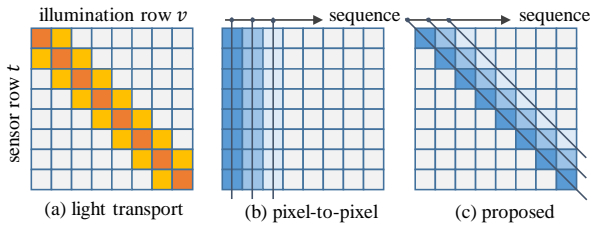


Fig. 21 Light transport matrix and the order of the acquisition. For the acquisition of light transport in scene (a), pixel-to-pixel measurement (b) is not efficient because it acquires light transport from a specific illumination row to all sensor rows at a single frame. In contrast, proposed measurement acquires light transport from illumination rows to sensor rows of the specific transport distance at a single frame.

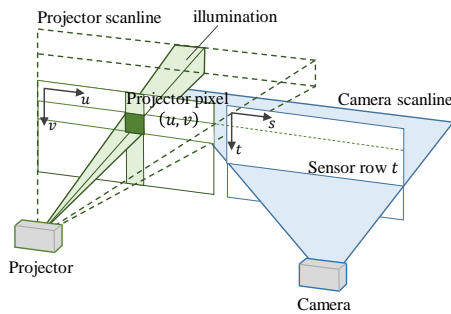


Fig. 22 Illustration of full light transport acquisition. A vertical stripe is employed to limit the illumination area to the certain pixel.

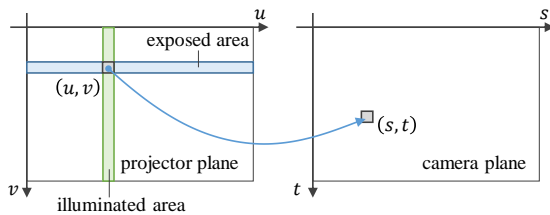


Fig. 23 Full Light Transport is defined as transport an illuminated pixel to a sensor pixel.

as shown in Fig. 23, the light transport $T_{full}(u, v, s, t)$ from a projector pixel (u, v) to a camera pixel (s, t) is acquired.

3.4 Hardware

We use a prototype as shown in Fig. 24. A Celluon PicoPro projector (resolution 1280×720) and an IDS UI-3250CP (resolution 1600×1200) are aligned on the same plane in parallel with a baseline of 50 mm. The rolling shutter is triggered by the VSYNC signal generated by the projector after being processed by the sync circuit. The speed of the projector scanline $v_p = 5.89 \times 10^3$ is obtained by counting a number of illuminated rows during fixed exposure.

3.5 Experiment

3.5.1 Analysis using full light transport

Using full light transport, we can perform more detailed analysis. In the case of full light transport, the profile at each pixel is two dimensional since it is a slice of $T_{full}(u, v, s_0, t_0)$, where s_0, t_0 are fixed to camera pixel. In Fig. 25, we show the profile of the different light transport in the scene. The diffuse reflection

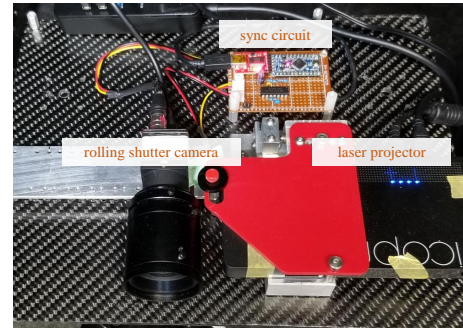


Fig. 24 Prototype. Rolling shutter of the camera and the raster-scan of the projector is synchronized by sync circuit.

from the book has clear rectangle shape (blue), since it is almost an impulse response to the rectangle illumination; Note that the delay profile has a clear unimodal peak. The subsurface scattering from wax candle (yellow) has larger extent compared with the surface of the book, and is isotropic. In the profile of diffuse inter-reflection from the corner of the book (green), we can see the advantage of the full light transport. It has large extent in the horizontal direction since the inter-reflection takes place between the left and right pages, therefore we can know the direction of inter-reflection. Also, the value of profile gradually decreases according to the distance from the center because the effect of the diffuse inter-reflections is depend on the distance between the surface. Finally, the specular inter-reflection from the disco-ball (purple) shows two independent clear peaks in the profile. From the profile, we can know the spatial relationship of the source of inter-reflection.

3.5.2 Appearance capture for graphics

Acquire light transport can be applied for graphics rendering. In this experiment, we acquire the plane-to-ray light transport of soap (Fig. 26(a)), that exhibit spatially-varying subsurface scattering. We render the models with the effect of subsurface scattering, and without the effect for the comparison. Specular reflection is attached as a post process for better perception. We assume the effect of subsurface scattering depends only on the transport distance, and the effect can be approximated by the delay sweep profile.

The result of teapot and bunny are shown in Fig. 26(a), (c) (with subsurface effect), and (b), (d) (without effect) respectively. The object is lit with a point light at left top. We can see the light blooming due to the effect of subsurface scattering, which is significant in the right half of teapot, and ears of the bunny.

3.5.3 Material classification using plane-to-ray light transport

The use of delay and exposure can yield fundamental new information about light scattering in materials, particularly subsurface scattering. Previous researchers have used time-of-flight measurements to achieve a similar result [28], [29]. Consider the delay profile for a given material. We expect the maximum of this plot to be at $t_d = 0$. However, our intuition is that the more subsurface scattering present in the material, the more spread out the delay profile will be.

In Fig. 27(a), we tested this hypothesis and its usefulness for material recognition of subsurface scattering in common house-

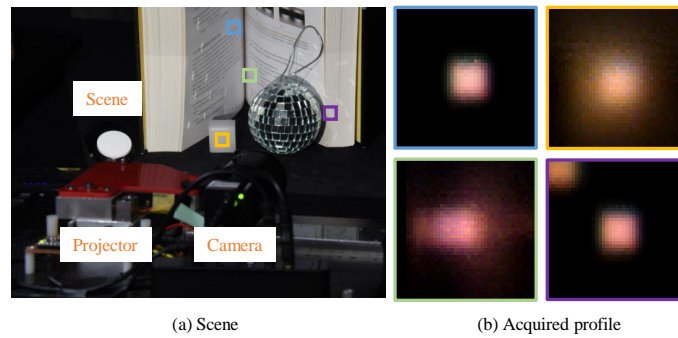


Fig. 25 Two dimensional profiles for various kinds of light behavior. They provides a spatial response that is useful for detailed analysis.

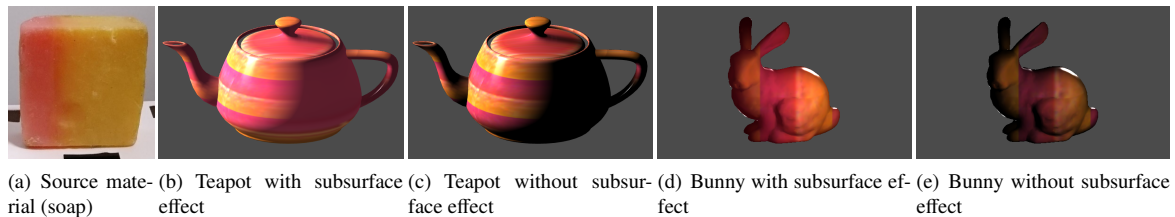


Fig. 26 Appearance capture for graphics. We transfer source material (a) to teapot and bunny models. Directional light is cast from left side in teapot scene, and from top-right in bunny scene. By including subsurface effect (b), (d), the areas which are not directly illuminated became brighter compared to image rendered without the effect (c), (e).

hold items. We imaged hand soap, fat free, 2%, and whole milk, and toothpaste. All of these items were white in color, and difficult to identify with RGB information alone. We plotted their average delay profiles for a set of their pixels shown in Fig. 27(b). We normalized these delay profiles using the area under the curve to cancel out the effects of albedo.

Using training and test images, we trained a support vector machine (SVM) with nonlinear kernel (radial Gaussian basis function) to get a per-pixel semantic segmentation of the materials (Fig. 27(c)) and a confusion matrix (Fig. 28). We achieved over 90% recognition for all the materials. We note that the only errors occurred for pixels near the edge of the container, where possibly the scattering profile changes for the materials due to the asymmetry of a boundary condition. This is an interesting avenue of future research to use delay profiles to better model or inverse render subsurface scattering. This application is not meant for robust instance-level material recognition, but highlights the usefulness of delay profiles for understanding subsurface scattering in materials.

3.5.4 Full light transport acquisition of various materials

Finally, we acquire the full light transport profile of several materials in Fig. 29. We use $l_w = 10\text{px}$, $l_d = 5\text{px}$ to $l_d = 995\text{px}$ at every 1px , $t_e = 170\mu\text{s}$, and $t_d = -340\mu\text{s}$ to $t_d = 340\mu\text{s}$ at every $17\mu\text{s}$. Each profile describes the transport to pixels shown in the appearance, from the relative illumination positions. Profiles have 41 columns and 41 rows that correspond to approximately $10\text{mm} \times 10\text{mm}$ in physical size. Profile values are normalized by its maximum after adjusting the white balance.

Let us take a look at the profile of materials shown in Fig. 29. (a) is the profile of a wooden ball that is considered to have Lambertian surface. The profile is isotropic and has small extent. (b) candle are the examples of subsurface scattering materials. It has

a larger extent than the that of the wooden ball. (c) is a cube whose surface exhibit a diffuse reflection and little specular reflection. The profiles are similar to diffuse surface at (c1) and (c2), and at (c) we can see a effect of inter-reflection between floor. (d) is a fake apple that is made of Styrofoam and covered with the surface with texture. We can see the shape of the profiles are the same at (d1), (d2), and (d3), beside the colors are different. (e) sponge and (f) marble are the examples of heterogeneous materials. In the profile of sponge, the profiles of pink (d1) and red (d2) pixels have similar extent because the scattering property of the material are same, while the color are different from each other. In the profile of marble, the pixel (f1) has slightly wider extent compared to (f2) since the each composition has different scattering property. Finally, (g) is the example of inhomogeneous materials. A miniature of the Jeditte Cabbage is made of plastic whose color are gradually changing from green to white (left to right). At (g1) almost all the pixels are green and at (g3) all the pixels are white. The profile at (g2) is the mixture of the green and the white pixel since the incident light reached in both green and white surfaces contribute to the pixel (g2).

4. Conclusion

In this thesis, we discussed about the light transport acquisition and the application of acquired light transport. Light transport is complicating process relating to the geometry of the scene and light behavior. The problem is how we acquire desired light transport in the presence of undesired light transport. To deal with this problem, we propose the selective path measurement. We specify paths by considering the geometry and the measurement setup, and selectively acquire the light transport along the path. Also proposal of analysis and application of light transport is our contribution.

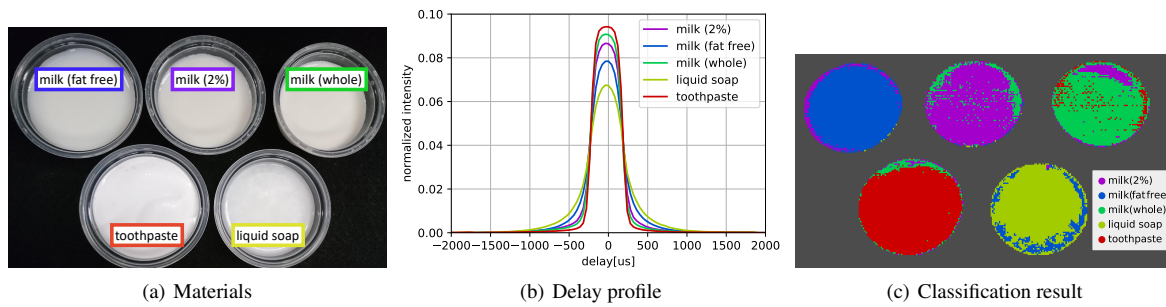


Fig. 27 Material classification using plane-to-ray light transport. We hardly classify the materials from the color image (a). However, delay profiles are clearly different (b), therefore, they are classified at the most pixels (c).

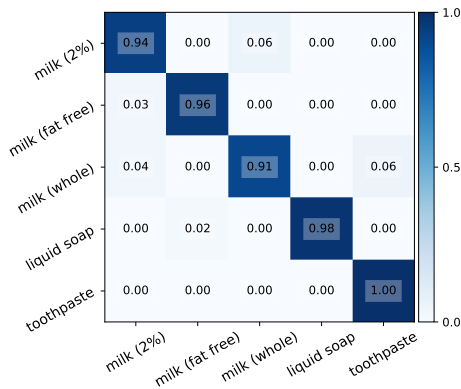


Fig. 28 Confusion matrix (Non-linear SVM). We achieved over 90% recognition for all the materials.

In Sec. 2, we tackle an optical tomography of diffuse surface object that has a diffuse surface and a transparent body. To reconstruct the interior of the object, light paths are required to be specified. We have proposed the shortest path model to represent light path in diffuse surface object. We have proposed the acquisition of light transport along shortest path and the reconstruction algorithm. We have performed simulation and real-world experiment to show the validity of our method.

In Sec. 3, we tackle light transport acquisition of projector camera system. For the efficient acquisition of light transport, we have proposed acquisition according to transport distance using synchronized projector camera system. We have proposed plane-to-ray light transport that is closely related to the synchronized system. The plane-to-ray light transport is acquired efficiently by synchronizing the rolling-shutter of a camera to a fixed offset of the raster-scan of projector in vertical direction. The acquisition have been extended to the acquisition of the full light transport by projecting a vertical line to acquire light transport in horizontal direction. We have shown visualization and application using the acquired light transport. We have shown analysis of light behavior, material classification, and appearance capture for computer graphics.

There are some limitations in our methods. For the problem of optical tomography, we have assumed the diffuse surface object. The effect of scattering and inter-reflection in the object degrades the reconstruction. For the acquisition in projector-camera system, the projector and camera are in rectified stereo setup. It results in the difficulty to acquire transport with angular variations.

Finally, we would like to show future direction of our work.

One possible direction is to explore the other dimensions of the plenoptic function. We have only considered the location and the angular of the light. A wavelength is interesting domain since the spectral response is related to the chemical substance and fluorescence that could found practical applications in the medical inspection or the food production. A time domain is also interesting since the temporal response is a great cue of scene understanding as some recent work reveal.

Like we utilized synchronized projector camera, light transport acquisition is closely related to hardware. There are lot of conventional and emerging hardware to combine, such like MEMS mirror, multi-bucket sensor [30], and angle sensitive pixel [31], [32]. The utilization of such hardware may allow us to novel acquisition of light transport.

We believe our concept of selective path measurement is a general framework that extends the possibility of scene analysis and further applications.

Acknowledgments This work was partly supported by JSPS KAKENHI Grant Numbers JP26700013, JP15K16027, JP15H05918, JP17K19979, JST CREST JPMJCR1764, and Foundation for Nara Institute of Science and Technology

References

- [1] Will, P. and Pennington, K.: Grid coding: A preprocessing technique for robot and machine vision, *Artificial Intelligence*, Vol. 2, No. 3, pp. 319–329 (1971).
- [2] Minou, M., Kanade, T. and Sakai, T.: A Method of Time-Coded Parallel Planes of Light for Depth Measurement, *Trans. Institute of Electronics and Communication Engineers of Japan*, Vol. E64, No. 8, pp. 521–528 (1981).
- [3] Woodham, R. J.: Photometric Method For Determining Surface Orientation From Multiple Images, *Optical Engineering*, Vol. 19, No. 1, pp. 139–144 (1980).
- [4] Horn, B. K. P.: Obtaining Shape from Shading Information, *Shape from Shading*, pp. 123–171 (1989).
- [5] Alpers, W. R., Ross, D. B. and Rufenach, C. L.: On the detectability of ocean surface waves by real and synthetic aperture radar, *Journal of Geophysical Research*, Vol. 86, No. C7, pp. 6481–6498 (1981).
- [6] Gupta, M., Agrawal, A., Veeraraghavan, A. and Narasimhan, S. G.: Structured light 3D scanning in the presence of global illumination, *Proceedings of the IEEE Conference on Computer Vision and Pattern Recognition (CVPR)*, pp. 713–720 (2011).
- [7] Chen, T., Lensch, H. P. A., Fuchs, C. and Seidel, H.: Polarization and Phase-Shifting for 3D Scanning of Translucent Objects, *Proceedings of the IEEE Conference on Computer Vision and Pattern Recognition (CVPR)*, pp. 1–8 (2007).
- [8] Gupta, M., Narasimhan, S. G. and Schechner, Y. Y.: On controlling light transport in poor visibility environments, *Proceedings of the IEEE Conference on Computer Vision and Pattern Recognition (CVPR)*, pp. 1–8 (2008).
- [9] Rowe, M. P., Pugh, E. N., Tyo, J. S. and Engheta, N.: Polarization-difference imaging: a biologically inspired technique for observation

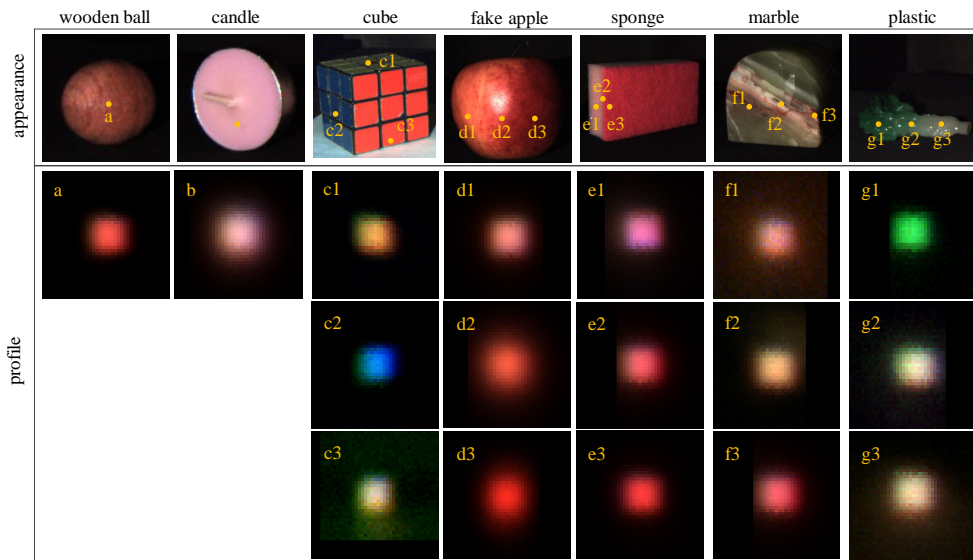


Fig. 29 Appearance and profiles of various materials. Profiles shows difference due to light behavior such like diffuse reflections, or subsurface scattering, and spatial variation.

through scattering media, *Optics Letters*, Vol. 20, No. 6, pp. 608–610 (1995).

[10] Iwaguchi, T., Funatomi, T., Kubo, H. and Mukaigawa, Y.: Light Path Alignment for Computed Tomography of Scattering Material, *IPSJ Transactions on Computer Vision and Applications*, Vol. 8, No. 1, p. 2 (2016).

[11] Iwaguchi, T., Funatomi, T., Aoto, T., Kubo, H. and Mukaigawa, Y.: Optical Tomography based on Shortest-path Model for Diffuse Surface Object, *IPSJ Transactions on Computer Vision and Applications*, Vol. 10, No. 1, p. 15 (2018).

[12] Laurentini, A.: The visual hull concept for silhouette-based image understanding, *IEEE Transactions on Pattern Analysis and Machine Intelligence (TPAMI)*, Vol. 16, No. 2, pp. 150–162 (1994).

[13] Parker, D. L.: Optimal short scan convolution reconstruction for fan beam CT, *Medical Physics*, Vol. 9, No. 2, pp. 254–257 (1982).

[14] Zeng, G. L.: The fan-beam short-scan FBP algorithm is not exact, *Physics in Medicine and Biology*, Vol. 60, No. 8, pp. 131–139 (2015).

[15] Gordon, R., Bender, R. and Herman, G. T.: Algebraic reconstruction techniques (ART) for three-dimensional electron microscopy and X-ray photography, *Journal of theoretical Biology*, Vol. 29, No. 3, pp. 471–481 (1970).

[16] Andersen, A. H. and Kak, A. C.: Simultaneous algebraic reconstruction technique (SART): a superior implementation of the ART algorithm, *Ultrasonic imaging*, Vol. 6, No. 1, pp. 81–94 (1984).

[17] Medoff, B. P., Brody, W. R., Nassi, M. and Macovski, A.: Iterative convolution backprojection algorithms for image reconstruction from limited data, *Journal of the Optical Society of America*, Vol. 73, No. 11, pp. 1493–1500 (1984).

[18] Delaney, A. H. and Bresler, Y.: A fast and accurate Fourier algorithm for iterative parallel-beam tomography, *IEEE Transactions on Image Processing*, Vol. 5, No. 5, pp. 740–753 (1996).

[19] Noo, F., Clackdoyle, R. and Pack, J.: A two-step Hilbert transform method for 2D image reconstruction, *Physics in Medicine and Biology*, Vol. 49, No. 17, pp. 3903–3923 (2004).

[20] Defrise, M., Noo, F., Clackdoyle, R. and Kudo, H.: Truncated Hilbert transform and image reconstruction from limited tomographic data, *Inverse Problems*, Vol. 22, No. 3, p. 1037 (2006).

[21] LaRoque, S. J., Sidky, E. Y. and Pan, X.: Accurate image reconstruction from few-view and limited-angle data in diffraction tomography, *Journal of the Optical Society of America*, Vol. 25, No. 7, pp. 1772–1782 (2008).

[22] Chen, G.-H., Tang, J. and Leng, S.: Prior image constrained compressed sensing (PICCS): A method to accurately reconstruct dynamic CT images from highly undersampled projection data sets, *Medical Physics*, Vol. 35, No. 2, pp. 660–663 (2008).

[23] Kubo, H., Jayasuriya, S., Iwaguchi, T., Funatomi, T., Mukaigawa, Y. and Narasimhan, S. G.: Acquiring and Characterizing Plane-to-Ray Indirect Light Transport, *Proceedings of the International Conference on Computational Photography (ICCP)*, pp. 1–10 (2018).

[24] Iwaguchi, T., Kubo, H., Funatomi, T., Mukaigawa, Y. and Narasimhan, S. G.: Acquiring Short Range 4D Light Transport with Synchronized Projector Camera System, *Proceedings of ACM Symposium on Virtual Reality Software and Technology (VRST)* (2018).

[25] Reddy, D., Ramamoorthi, R. and Curless, B.: Frequency-space Decomposition and Acquisition of Light Transport Under Spatially Varying Illumination, *Proceedings of the European Conference on Computer Vision (ECCV)*, pp. 596–610 (2012).

[26] O’Toole, M., Achar, S., Narasimhan, S. G. and Kutulakos, K. N.: Homogeneous Codes for Energy-efficient Illumination and Imaging, *ACM Transactions on Graphics (ToG)*, Vol. 34, No. 4, pp. 1–13 (2015).

[27] Sen, P., Chen, B., Garg, G., Marschner, S. R., Horowitz, M., Levoy, M. and Lensch, H. P. A.: Dual photography, *ACM Transactions on Graphics (ToG)*, Vol. 24, No. 3, pp. 745–755 (2005).

[28] Su, S., Heide, F., Swanson, R., Klein, J., Callenberg, C., Hullin, M. and Heidrich, W.: Material classification using raw time-of-flight measurements, *Proceedings of the IEEE Conference on Computer Vision and Pattern Recognition (CVPR)*, pp. 3503–3511 (2016).

[29] Wu, D., Velten, A., O’toole, M., Masia, B., Agrawal, A., Dai, Q. and Raskar, R.: Decomposing global light transport using time of flight imaging, *International Journal of Computer Vision*, Vol. 107, No. 2, pp. 123–138 (2014).

[30] Wan, G., Li, X., Agranov, G., Levoy, M. and Horowitz, M.: CMOS Image Sensors With Multi-Bucket Pixels for Computational Photography, *IEEE Journal of Solid-State Circuits*, Vol. 47, No. 4, pp. 1031–1042 (2012).

[31] Hirsch, M., Sivaramakrishnan, S., Jayasuriya, S., Wang, A., Molnar, A., Raskar, R. and Wetzstein, G.: A switchable light field camera architecture with Angle Sensitive Pixels and dictionary-based sparse coding, *Proceedings of the International Conference on Computational Photography (ICCP)*, pp. 1–10 (2014).

[32] Wang, A., Gill, P. and Molnar, A.: Angle sensitive pixels in CMOS for lensless 3D imaging, *IEEE Custom Integrated Circuits Conference*, pp. 371–374 (2009).